Finite Element Analysis of Rock Deformation in Deep Twin Tunnels

Felipe P. M. Quevedo[1], Carlos A. M. M. Colombo[1], Bianca M. Girardi[1], Denise Bernaud[1], Samir Maghous[1]

[1]*Graduate Program in Civil Engineering, Federal University of Rio Grande do Sul*
Av. Osvaldo Aranha, 99, Porto Alegre, 90.035-190, RS, Brazil
motta.quevedo@ufrgs.br, ca-colombo@hotmail.com, eng.biancagirardi@gmail.com
denise.bernaud@ufrgs.br, samir.maghous@ufrgs.br

Abstract. Relying upon a three-dimensional finite element analysis, this contribution investigates the instantaneous irreversible response induced by the constitutive behavior of the rock mass in the convergence profile of twin tunnels with transverse gallery. At the rock material level, elastoplastic state equations based on a Drucker-Prager yield surface with an associated flow rule are adopted in the modeling. As regards the tunnel support, the formulation accounts for the presence of an elastic shotcrete-like lining. From a computational point of view, the deactivation-activation method is used to simulate the excavation process and the installation of the lining. The accuracy of the finite element predictions is assessed through comparisons with the available analytical solutions formulated in a simplified scenario for the twin tunnel configuration. A parametric study investigates the mutual interaction induced by the proximity of the tunnels and the influence of the lining stiffness.

Keywords: Twin tunnels, Transverse gallery, Elastoplasticity, Finite element modeling

1 Introduction

Many design methods often focus on single tunnels, but twin tunnels are a common occurrence. The interaction between tunnels can be significant, especially when the spacing between them is minimal. Additionally, many twin tunnels incorporate transverse galleries, introducing a localized effect on displacements and stresses. While the simulation of tunnel convergence in single tunnels has been widely investigated and reported in published literature, few works have addressed the computational evaluation of deformation in twin tunnels. Some studies on deep twin tunnels can be found at Spyridis and Bergmeister [1], Chen et al. [2], Ma et al. [3], Fortsakis et al. [4], Chortis and Kavvadas [5], Chortis and Kavvadas [6], Guo et al. [7], Chortis and Kavvadas [8], Chortis and Kavvadas [9]. However, less attention has been dedicated to assessing the mutual mechanical interaction induced by the excavation of the transverse gallery connecting the twin tunnels.

In this context, the main contributions of this paper can be summarized at both the material and tunnel analysis levels. At the material level, the constitutive state equations of deep rock mass are developed using a plasticity framework, which is suitable for clayey rocks. For the mechanical behavior of the concrete lining, the traditional linear elastic model is employed. At the structural analysis level, the deformation of the highly interactive components of the material system (i.e., rock mass and lining) resulting from the excavation of twin tunnels and transverse gallery is simulated using three-dimensional finite element simulations. The excavation and lining placement processes are simulated through the activation/deactivation technique. The constitutive models for the rock mass and the associated numerical integration schemes are implemented into the UPF/USERMAT customization tool [10] of the ANSYS standard software. This three-dimensional finite element analysis is specifically designed to address the interactions induced by the construction process, the proximity of twin tunnels, and the presence of the transverse gallery.

2 Constitutive Models

The constitutive model for the rock mass corresponds to the associated Drucker-Prager elastoplastic model. The local strain rate $\dot{\boldsymbol{\varepsilon}}$ is split into two contributions $\dot{\boldsymbol{\varepsilon}} = \dot{\boldsymbol{\varepsilon}}^e + \dot{\boldsymbol{\varepsilon}}^p$, so that the constitutive relationships relating the Cauchy stress rate $\dot{\boldsymbol{\sigma}}$ and strain rate components can be written as:

$$\dot{\boldsymbol{\sigma}} = \boldsymbol{D} : \dot{\boldsymbol{\varepsilon}}^e = \boldsymbol{D} : (\dot{\boldsymbol{\varepsilon}} - \dot{\boldsymbol{\varepsilon}}^p). \tag{1}$$

In the above relationship, $\dot{\boldsymbol{\varepsilon}}^e$ and $\dot{\boldsymbol{\varepsilon}}^p$, represent respectively the elastic and plastic strain rate, and $\boldsymbol{D}$ denote the fourth-order isotropic elastic linear constitutive tensor defined by the rock mass elastic Young modulus E and Poisson ratio ν. The plastic strain rate is given by the flow rule:

$$\dot{\boldsymbol{\varepsilon}}^p = \begin{cases} \dot{\lambda}\dfrac{\partial g}{\partial \boldsymbol{\sigma}} & \text{for } f > 0 \\ \boldsymbol{0}, & \text{for } f \leq 0 \end{cases}, \tag{2}$$

where $\dot{\lambda}$ is the plasticity multiplier (obtained through the consistency condition $\dot{f} = 0$) and g is a potential flow function analogous to f used to simulate the volume dilatation during the evolution of plastic deformations. However, for this analysis, associated plasticity was adopted, i.e., $g = f$. In this model, the Drucker-Prager plastic flow surface is given by

$$f(\boldsymbol{\sigma}, q) = f(I_1, J_2, q) = \beta_1 I_1 + \beta_2 \sqrt{J_2} - q(\alpha), \tag{3}$$

which I_1 is the first invariant of the stress tensor, J_2 is the second invariant of the deviator tensor and β_1, β_2 and $q(\alpha)$ are strength parameters related to the friction angle ϕ and cohesion $c(\alpha)$, respectively. The Drucker-Prager plasticity surface inscribed in the Mohr-Coulomb surface is considered, i.e. [11]:

$$\beta_1 = \frac{(k-1)}{3}, \quad \beta_2 = \frac{(2k+1)}{\sqrt{3}}, \quad q(\alpha) = 2\sqrt{k}\,c(\alpha), \tag{4}$$

where $k = (1 + \sin \phi)/(1 - \sin \phi)$. The internal variable α is the equivalent plastic strain $\bar{\varepsilon}^p$ used to simulate strain hardening/softening phenomena. However, for this study, we adopt perfect plasticity, meaning that c is a constant.

A linear elastic constitutive model is used for the concrete lining, which can be expressed, within the framework of infinitesimal analysis, as $\dot{\boldsymbol{\sigma}} = \boldsymbol{D} : \dot{\boldsymbol{\varepsilon}}^e$, where, $\dot{\boldsymbol{\varepsilon}}^e$ and $\boldsymbol{D}$ are respectively the elastic strain rate and the fourth-order isotropic elastic constitutive tensor defined by the concrete lining Poisson ratio ν_c and elastic Young modulus E_c. In the analyses, for comparisons, the tunnel stiffness will be given by the following expression [12]:

$$K_c = \frac{E_c}{1 + \nu_c} \frac{R_t^2 - (R_t - e_t)^2}{(1 - 2\nu_c)R_t + (R_t - e_t)^2}, \tag{5}$$

where R_t is the tunnel radius and e_t is the tunnel wall thickness.

3 Spatial discretization of the domain

The material domain Ω for finite element simulations is defined as a parallelepiped with dimensions $(L_1 + L_2) \times L_3 \times d_3$ (see Fig. 1). Due to symmetry, only the material portion in the region $\{x \leq 0, y \geq 0\}$ is discretized for F.E. analysis. In Fig. 1, d_1 represents the distance between the axes of longitudinal tunnels, L_2 is the total excavated length along longitudinal direction $\boldsymbol{e}_z$, d_3 is the domain thickness along vertical direction $\boldsymbol{e}_y$, L_1 is the length of the unexcavated region after tunneling, L_3 is the domain length along transversal direction $\boldsymbol{e}_x$, and d_2 indicates the position of the transverse gallery axis that intersects the longitudinal tunnel at $z = L_1 + d_2$.

The mesh used consists of either 119740 or 221104 total elements (hexahedra and tetrahedra), depending on the longitudinal tunnel spacing d_1. To enhance model accuracy in the intersection zone, 10-node quadratic tetrahedral elements are used around the transverse gallery, while 8-node trilinear hexahedral elements are employed in the rest of the domain. Regions significantly influenced by tunneling are highlighted in light gray in Fig. 1. Two values of d_1 are considered in the parametric simulations: $d_1 = 16R_t$ and $4R_t$.

The concrete lining along the gallery wall, shown in red in Fig. 1, has a thickness e_g. The gallery radius R_g is fixed at $2/3R_t$ for simplicity, with the same lining system (same concrete material and layer thickness) applied to both longitudinal tunnels. Parameters d_5 and d_1 define the size of the transition region involving tetrahedral elements in the yz plane around the gallery.

The initial stress state prevailing in the rock mass prior to the tunnel excavation process is defined by constant vertical and horizontal geostatic stress σ_v and σ_h taking the following form:

$$\boldsymbol{\sigma}_0 = -\sigma_v \boldsymbol{e}_y \otimes \boldsymbol{e}_y - \sigma_h \left(\boldsymbol{1} - \boldsymbol{e}_y \otimes \boldsymbol{e}_y\right) \tag{6}$$
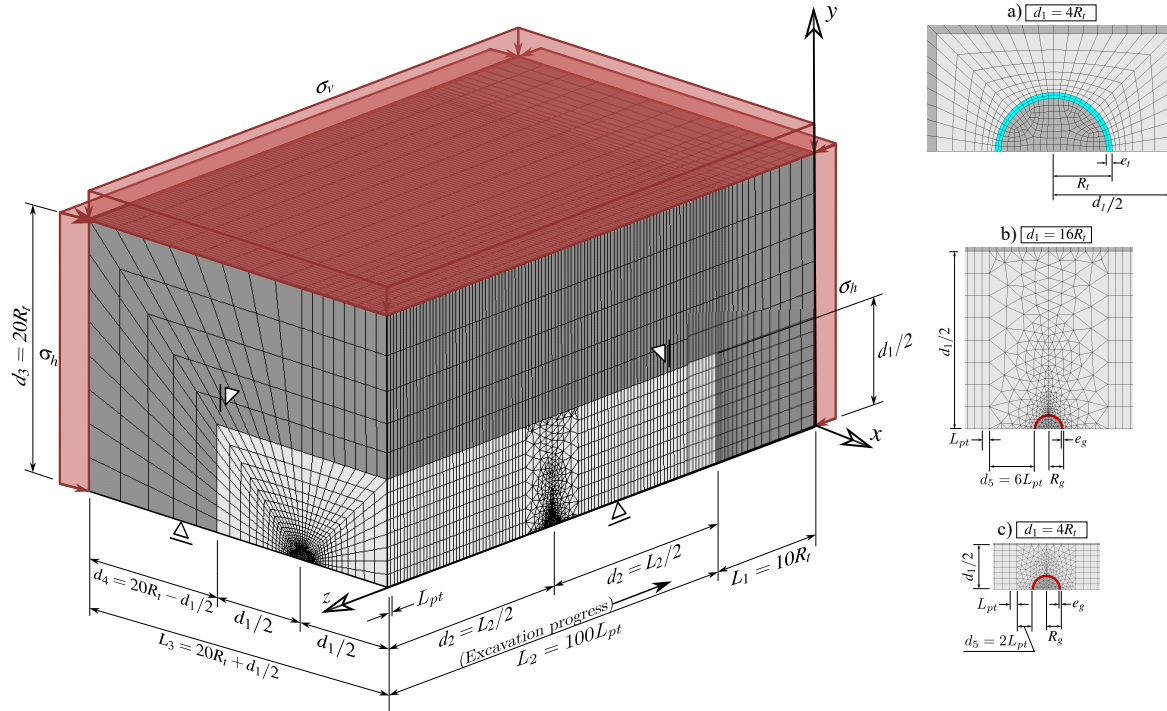
Figure 1. Geometry, mesh and boundary conditions of domain and details of a) longitudinal tunnel cross-section for configuration $d_1 = 4R_t$ and gallery cross-section for configurations b) $d_1 = 16R_t$ and c) $d_1 = 4R_t$.

As mentioned previously, the tunneling process, including the excavation steps and lining installation, is simulated by resorting to the activation-deactivation method shown in the schematic representation in Fig. 2. Each excavation step is modeled by deactivation of the corresponding elements (the elements stiffness is reduced by a factor $1E8$), whereas installation of elements of lining at a distance d_{0t} from the excavation face (unlined length) is achieved through activation of the corresponding elements by assigning them concrete properties. In this figure, n_p is the total number of excavation steps and n_{pig} represents the number of longitudinal tunnel excavation steps before gallery excavation. After achievement of the n_{pig} excavation steps, the excavation of the gallery is initiated starting from the longitudinal tunnel wall. Referring to the notation of Fig. 2, L_{pg} is the considered step length for the gallery excavation, and d_{0g} is the unlined length of the gallery. After the gallery excavation is completed, we proceed to further excavation steps of the longitudinal tunnel. The main parameters defining the geometry domain as well as the excavation process and lining installation are summarized in Table 1.
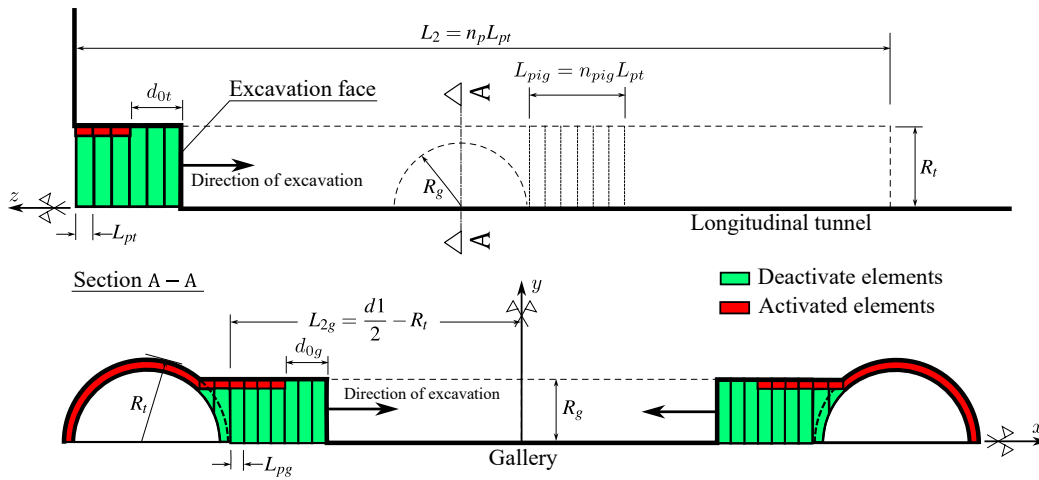

Figure 2. Schematic representation of the excavation process.

Table 1. Parameters related to the geometry of the domain, excavation and installation of the lining.

PARAMETERS	SYMBOL	UNIT	VALUES
Longitudinal tunnels			
Radius of the longitudinal tunnel	R_t	m	R_t
Thickness of the lining	e_t	m	$0.1R_t, 0.03R_t$
Length of the excavation step	L_{pt}	m	$1/3R_t$
Unlined length	d_{0t}	m	$2L_{pt}$
Gallery			
Radius of the gallery	R_g	m	$2/3R_t$
Thickness of the lining	e_g	m	e_t
Length of the excavation step	L_{pg}	m	$1/3R_g$
Unlined length	d_{0g}	m	$2L_{pg}$
Number of steps that starts gallery excavation	n_{pig}	un	15
Rest of domain			
Distance between longitudinal tunnel axes	d_1	m	$4R_t,\ 16R_t$
Total length along vertical direction $\boldsymbol{e}_y$	d_3	m	$20R_t$
Length of unexcavated region	L_1	m	$10R_t$
Total excavated length	L_2	m	$100L_{pt}$
Total length along transversal direction $\boldsymbol{e}_x$	L_3	m	$20R_t + d_1/2$

4 Verification with unlined twin tunnel in elastoplastic medium

In the context of plane strain conditions, Ma et al. [3] developed an approximate analytical solution for the stresses and the plastic zone boundary around deep twin circular tunnels excavated in a homogeneous elastoplastic medium. For the constitutive model, the authors considered perfectly plastic Mohr-Coulomb criterion with associated plastic flow rule. The stress solution for twin tunnels was formulated on the premise that the plastic zone around each tunnel fully encloses the tunnel edge, with the two plastic zones remaining separate and unconnected.

Fig. 3 shows the comparison between the 3D F.E. Solution (from a far behind the excavation face) and the analytical solution for plastic zone boundary provided in [3]. For these analysis, $R_t = 1$ m, $d_1/2R_t = 2.5$, rock Young's modulus $E = 20$ GPa, Poisson's ratio $\nu = 0.3$ and, friction angle $\phi = 30°$. This analysis shows that finite element modeling produces predictions very similar with those shown in 3. In addition, the results show that lower values of cohesion c result in larger plastic zones.

$c = 2.5$ MPa, $\sigma_h = 30$ MPa, $\sigma_v = 30$ MPa $c = 5$ MPa, $\sigma_h = 40$ MPa, $\sigma_v = 30$ MPa

- - - - - Boundary of the plastic zone - Analytical Solution [3]
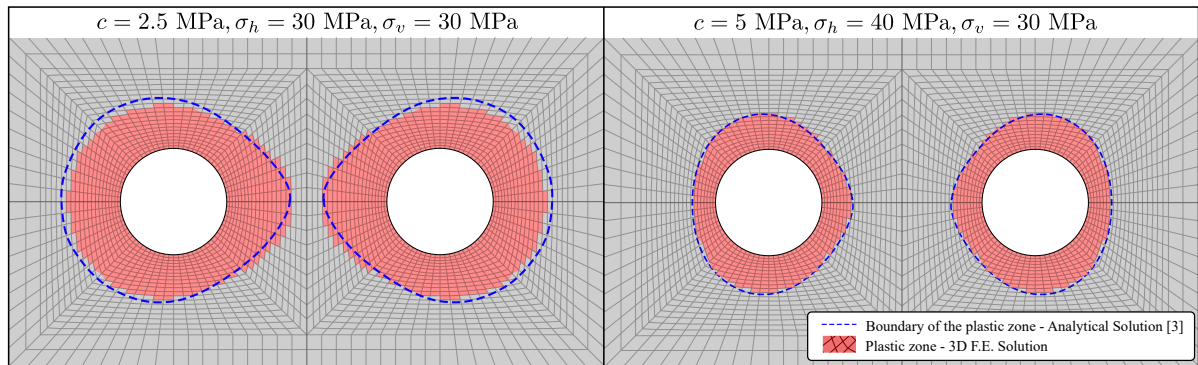Plastic zone - 3D F.E. Solution

Figure 3. The plastic zone extent obtained from the present F.E. simulations and from the stress solution provided in Ma et al. [3].

Further comparisons are illustrated in Fig. 4, which shows the radial σ_{rr} and orthoradial $\sigma_{\theta\theta}$ stress components along three radial paths defined in polar coordinates by $\theta = 45°$, $90°$, and $135°$. It is important to note that although the finite element simulations use the Drucker-Prager yield surface inscribed within the Mohr-Coulomb surface (as used in the solution by Ma et al. [3], the numerical predictions closely match the analytical stress solution.
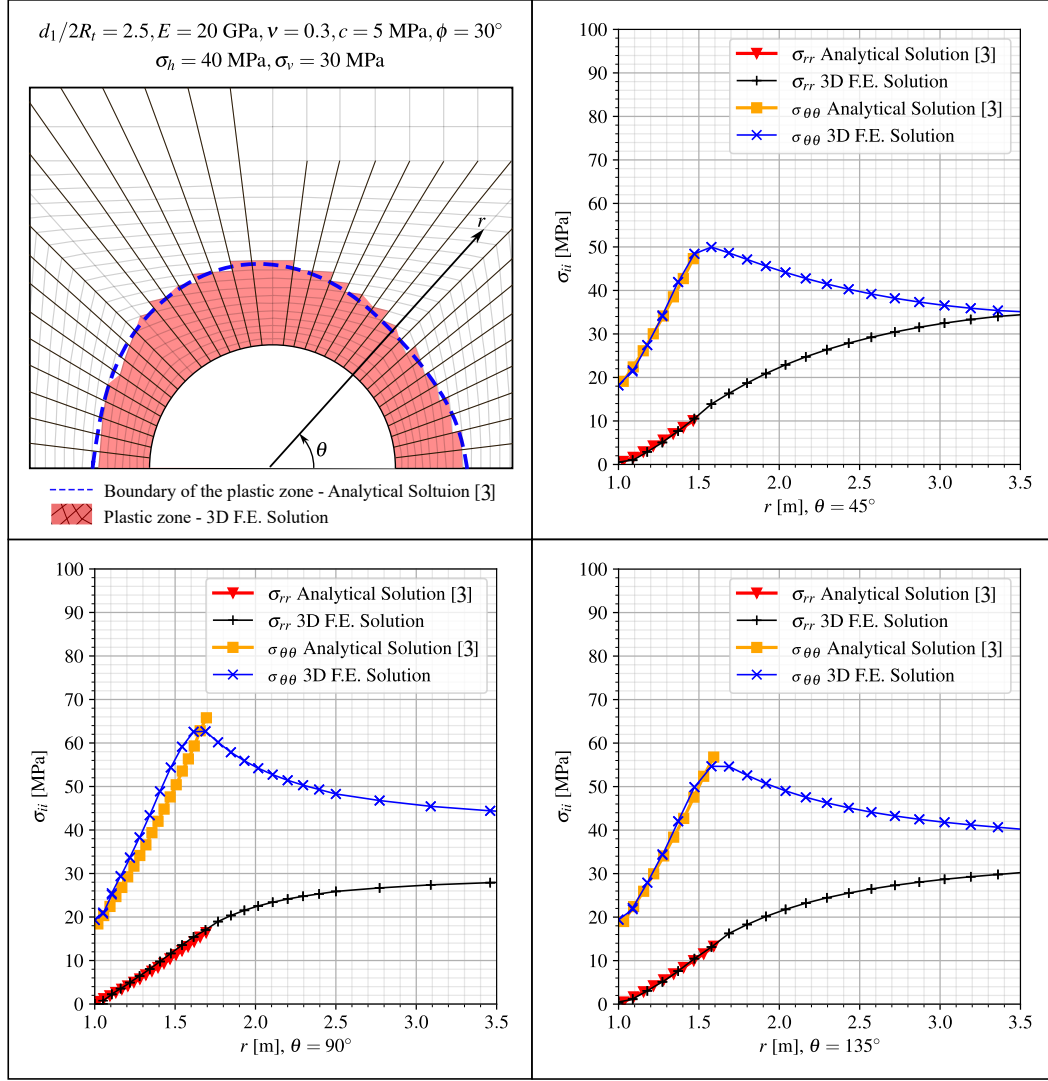
Figure 4. Distribution of radial and orthoradial stress components along different radial directions: comparison between numerical and analytical predictions.

.

5 Numerical Results and Discussion

To develop the analysis, we employed Young's modulus $E = 1500$ MPa, Poisson ratio $\nu = 0.49$, $c = 4\sqrt{3}/2$, $\phi = 0°$ and, isotropic initial stresses $\sigma_v = \sigma_h = 9$ MPa, which correspond to the constitutive parameters and tunneling conditions (450 m depth) in the incompressive clay rock mass in the Paris basin (in Aisne, France), as detailed in Rousset [13], Giraud [14] and, Piepi [15]. For the lining, two stiffness values will be considered: $K_c = 969$ MPa and $K_c = 3403$ MPa. Assuming a Young's modulus $E_c = 30303$ MPa and Poisson's ratio $\nu_c = 0.2$, these values corresponds to lining thicknesses e_t of $0.03R_t$ and $0.1R_t$.

Denoting by u_y the displacement component following the y-axis, Fig. 5 and Fig. 6 displays the convergence curves $U_B = -u_y(B)/R_t$ that characterize the inward movement at the tunnel roof $B(x = 0, y = R_t, z)$ as a function of normalized longitudinal distance to the facing for different conditions: without lining (NL), with elastic lining (EL), with (WG) and without gallary (NG) for $d_1 = 16R_t$ and $d_1 = 4R_t$. In these figures, U_C represents convergence at $z/R_t = -25$ (far from the effect of the excavation face and gallery), and U_D is highlighted at the gallery position $D(x = 0, y = R_t, z = L_2/2)$.

For the single tunnel, the higher stiffness lining (black solid line) reduced convergence by approximately 35% compared to the unlined scenario (black dashed line). Conversely, the moderately stiff lining (black dotted line) increased convergence by 12% compared to the higher stiffness lining.

When $d_1 = 16R_t$ (blue and yellow lines), the results of U_C are similar to the isolated tunnel (black line). However, with a distance reduced to $d_1 = 4R_t$, the interaction between the tunnels becomes significant. A smaller

d_1, the higher stiffness lining (solid yellow and blue lines) can restrict convergence by up to 46% of the unlined (dashed yellow and blue lines) convergence. A moderate stiffness lining (dotted lines) leads to an increase of up to 16% in convergence compared to the higher stiffness lining (solid lines).
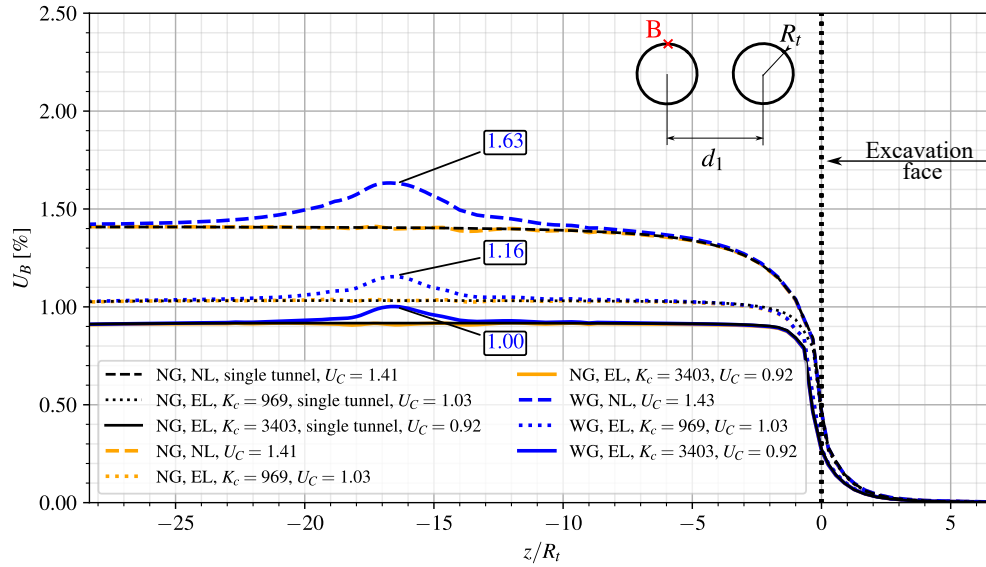

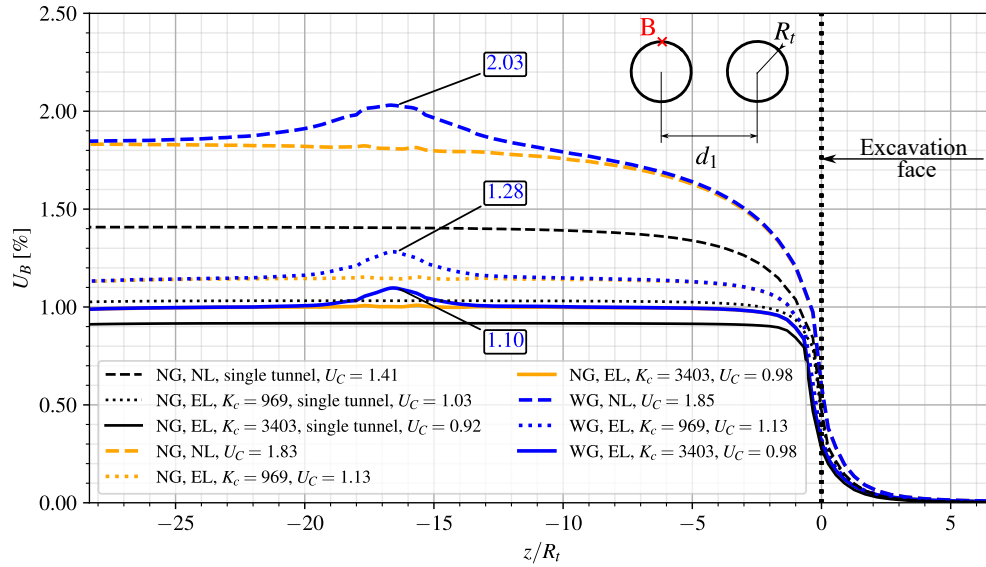Figure 5. Convergence Profiles at the tunnel roof (point B) - for $d_1 = 16R_t$.

.

Figure 6. Convergence Profiles at the tunnel roof (point B) - for $d_1 = 4R_t$.

.

When comparing results between twin lined tunnels with spacings of $16R_t$ and $4R_t$, differences of 6% with higher stiffness lining (solid yellow and blue lines), 10% with moderate stiffness lining (dotted yellow and blue lines), and 30% without lining (dashed yellow and blue lines) are observed. These results show the direct impact of lining stiffness and the distance between twin tunnels on U_C convergence.

When analyzing the convergence U_D at the point where the gallery meets the longitudinal tunnel, there is an increase of 16% when using an moderate stiffness lining (dotted blue line) compared to a higher stiffness lining (solid blue line). However, when analyzing the difference between the U_C and U_D, there is a difference of up to

12% for the higher stiffness lining (solid blue line to $4R_t$ and $16R_t$) and up to 13% for the moderate stiffness lining (dotted blue line to $4R_t$ and $16R_t$) for $d_1 = 4R_t$. In both figures, increased stiffness localizes the gallery's effect on the convergence profile, reducing it from $22.5R_g$ (without lining) to $10.5R_g$ and $7.5R_g$ (with lining) along the longitudinal tunnel. Tunnel proximity had minimal impact on this range.

6 Conclusions

Considering the constitutive parameters and tunneling conditions adopted, the analyses show that the lining has a profound impact on the convergence profile of the twin tunnels. It reduces overall convergence by up to 35% and diminishes the localized convergence of the gallery by approximately a third compared to unlined scenario. In addition, a less rigid lining, approximately 3.5 times less stiff, increases convergence by 12% and expands the localized effect by 40% compared to the stiffer lining. Tunnel interaction becomes significant at $4R_t$ however has minimal impact in the range of gallery's localized effect along the longitudinal tunnel.

Authorship statement. The authors hereby confirm that they are the sole liable persons responsible for the authorship of this work, and that all material that has been herein included as part of the present paper is either the property (and authorship) of the authors, or has the permission of the owners to be included here.

References

[1] P. Spyridis and K. Bergmeister. Analysis of lateral openings in tunnel linings. *Tunnelling and Underground Space Technology*, vol. 50, pp. 376–395, 2015.

[2] F. Chen, L.-b. Lin, and D. Li. Analytic solutions for twin tunneling at great depth considering liner installation and mutual interaction between geomaterial and liners. *Applied Mathematical Modelling*, vol. 73, 2019.

[3] Y. Ma, A. Lu, X. Zeng, and H. Cai. Analytical solution for determining the plastic zones around twin circular tunnels excavated at great depth. *International Journal of Rock Mechanics and Mining Sciences*, vol. 136, pp. 104475, 2020.

[4] P. Fortsakis, E. Bekri, G. Prountzopoulos, and P. Marinos. Numerical analysis of twin tunnels interaction. In *Proc. 1st Eastern European Tunnelling Conference*, Budapest, Hungary, 2012.

[5] F. Chortis and M. Kavvadas. Three-dimensional numerical analyses of perpendicular tunnel intersections. *Geotechnical and Geological Engineering*, vol. 39, pp. 1771–1793, 2021a.

[6] F. Chortis and M. Kavvadas. Three-dimensional numerical investigation of the interaction between twin tunnels. *Geotechnical and Geological Engineering*, vol. 39, pp. 5559–5585, 2021b.

[7] Z. Guo, X. Liu, and Z. Zhu. An elastic solution for twin circular tunnels' stress in hydrostatic stress field. *Geotechnical and Geological Engineering*, vol. 39, pp. 1–11, 2021.

[8] F. Chortis and M. Kavvadas. 3D numerical investigation of the axial forces acting on tunnel junctions constructed in fractured/weathered to very blocky rockmass. In *Expanding Underground-Knowledge and Passion to Make a Positive Impact on the World*, pp. 1574–1582. CRC Press, 2023a.

[9] F. Chortis and M. Kavvadas. 3D numerical investigation of the bending moments acting on tunnel junctions constructed in fractured/weathered to very blocky rockmass. In *Expanding Underground-Knowledge and Passion to Make a Positive Impact on the World*, pp. 1583–1591. CRC Press, 2023b.

[10] ANSYS. *ANSYS Programmer's Reference, release 15.0*. Canonsburg, Pennsylvania, 2013.

[11] D. Bernaud. *Tunnels profonds dans les milieux viscoplastiques: approches expérimentale et numérique*. Ph.D. Thesis (in french), Ecole Nationale des Ponts et Chaussées, Paris, France, 1991.

[12] M. Panet. *Le Calcul des Tunnels par la Méthode Convergence-Confinement*. Presses De L'ecole Nationale Des Ponts Et Chaussees, 1995.

[13] G. Rousset. *Comportement mecanique des argiles profondes: Application au stockage de déchets radioactifs*. Ph.D. Thesis (in french), Ecole Nationale des Ponts et Chaussées, Paris, France, 1988.

[14] A. Giraud. *Couplages thermo-hydro-mécaniques dans les poreux peu perméables: application aux argiles profondes*. Ph.D. Thesis (in french), Ecole Nationale des Ponts et Chaussées, Paris, France, 1993.

[15] G. T. Piepi. *Comportement viscoplastique avec rupture des argiles raides. Applications aux ouvrages souterrains*. Ph.D. Thesis (in french), Ecole Nationale des Ponts et Chaussées, Paris, France, 1995.